Elliptic flow from two- and four-particle correlations in Au+Au collisions at $\sqrt{s_{NN}} = 130$ GeV

C. Adler,[11] Z. Ahammed,[23] C. Allgower,[12] J. Amonett,[14] B. D. Anderson,[14] M. Anderson,[5] G. S. Averichev,[9] J. Balewski,[12] O. Barannikova,[9,23] L. S. Barnby,[14] J. Baudot,[13] S. Bekele,[20] V. V. Belaga,[9] R. Bellwied,[31] J. Berger,[11] H. Bichsel,[30] A. Billmeier,[31] L. C. Bland,[2] C. O. Blyth,[3] B. E. Bonner,[24] A. Boucham,[26] A. Brandin,[18] A. Bravar,[2] R. V. Cadman,[1] H. Caines,[33] M. Calderón de la Barca Sánchez,[2] A. Cardenas,[23] J. Carroll,[15] J. Castillo,[26] M. Castro,[31] D. Cebra,[5] P. Chaloupka,[20] S. Chattopadhyay,[31] Y. Chen,[6] S. P. Chernenko,[9] M. Cherney,[8] A. Chikanian,[33] B. Choi,[28] W. Christie,[2] J. P. Coffin,[13] T. M. Cormier,[31] J. G. Cramer,[30] H. J. Crawford,[4] W. S. Deng,[2] A. A. Derevschikov,[22] L. Didenko,[2] T. Dietel,[11] J. E. Draper,[5] V. B. Dunin,[9] J. C. Dunlop,[33] V. Eckardt,[16] L. G. Efimov,[9] V. Emelianov,[18] J. Engelage,[4] G. Eppley,[24] B. Erazmus,[26] P. Fachini,[2] V. Faine,[2] K. Filimonov,[15] E. Finch,[33] Y. Fisyak,[2] D. Flierl,[11] K. J. Foley,[2] J. Fu,[15,32] C. A. Gagliardi,[27] N. Gagunashvili,[9] J. Gans,[33] L. Gaudichet,[26] M. Germain,[13] F. Geurts,[24] V. Ghazikhanian,[6] O. Grachov,[31] V. Grigoriev,[18] M. Guedon,[13] E. Gushin,[18] T. J. Hallman,[2] D. Hardtke,[15] J. W. Harris,[33] T. W. Henry,[27] S. Heppelmann,[21] T. Herston,[23] B. Hippolyte,[13] A. Hirsch,[23] E. Hjort,[15] G. W. Hoffmann,[28] M. Horsley,[33] H. Z. Huang,[6] T. J. Humanic,[20] G. Igo,[6] A. Ishihara,[28] Yu. I. Ivanshin,[10] P. Jacobs,[15] W. W. Jacobs,[12] M. Janik,[29] I. Johnson,[15] P. G. Jones,[3] E. G. Judd,[4] M. Kaneta,[15] M. Kaplan,[7] D. Keane,[14] J. Kiryluk,[6] A. Kisiel,[29] J. Klay,[15] S. R. Klein,[15] A. Klyachko,[12] A. S. Konstantinov,[22] M. Kopytine,[14] L. Kotchenda,[18] A. D. Kovalenko,[9] M. Kramer,[19] P. Kravtsov,[18] K. Krueger,[1] C. Kuhn,[13] A. I. Kulikov,[9] G. J. Kunde,[33] C. L. Kunz,[7] R. Kh. Kutuev,[10] A. A. Kuznetsov,[9] L. Lakehal-Ayat,[26] M. A. C. Lamont,[3] J. M. Landgraf,[2] S. Lange,[11] C. P. Lansdell,[28] B. Lasiuk,[33] F. Laue,[2] A. Lebedev,[2] R. Lednický,[9] V. M. Leontiev,[22] M. J. LeVine,[2] Q. Li,[31] S. J. Lindenbaum,[19] M. A. Lisa,[20] F. Liu,[32] L. Liu,[32] Z. Liu,[32] Q. J. Liu,[30] T. Ljubicic,[2] W. J. Llope,[24] G. LoCurto,[16] H. Long,[6] R. S. Longacre,[2] M. Lopez-Noriega,[20] W. A. Love,[2] T. Ludlam,[2] D. Lynn,[2] J. Ma,[6] R. Majka,[33] S. Margetis,[14] C. Markert,[33] L. Martin,[26] J. Marx,[15] H. S. Matis,[15] Yu. A. Matulenko,[22] T. S. McShane,[8] F. Meissner,[15] Yu. Melnick,[22] A. Meschanin,[22] M. Messer,[2] M. L. Miller,[33] Z. Milosevich,[7] N. G. Minaev,[22] J. Mitchell,[24] V. A. Moiseenko,[10] C. F. Moore,[28] V. Morozov,[15] M. M. de Moura,[31] M. G. Munhoz,[25] J. M. Nelson,[3] P. Nevski,[2] V. A. Nikitin,[10] L. V. Nogach,[22] B. Norman,[14] S. B. Nurushev,[22] G. Odyniec,[15] A. Ogawa,[21] V. Okorokov,[18] M. Oldenburg,[16] D. Olson,[15] G. Paic,[20] S. U. Pandey,[31] Y. Panebratsev,[9] S. Y. Panitkin,[2] A. I. Pavlinov,[31] T. Pawlak,[29] V. Perevoztchikov,[2] W. Peryt,[29] V. A. Petrov,[10] M. Planinic,[12] J. Pluta,[29] N. Porile,[23] J. Porter,[2] A. M. Poskanzer,[15] E. Potrebenikova,[9] D. Prindle,[30] C. Pruneau,[31] J. Putschke,[16] G. Rai,[15] G. Rakness,[12] O. Ravel,[26] R. L. Ray,[28] S. V. Razin,[9,12] D. Reichhold,[8] J. G. Reid,[30] G. Renault,[26] F. Retiere,[15] A. Ridiger,[18] H. G. Ritter,[15] J. B. Roberts,[24] O. V. Rogachevski,[9] J. L. Romero,[5] A. Rose,[31] C. Roy,[26] V. Rykov,[31] I. Sakrejda,[15] S. Salur,[33] J. Sandweiss,[33] A. C. Saulys,[2] I. Savin,[10] J. Schambach,[28] R. P. Scharenberg,[23] N. Schmitz,[16] L. S. Schroeder,[15] A. Schüttauf,[16] K. Schweda,[15] J. Seger,[8] D. Seliverstov,[18] P. Seyboth,[16] E. Shahaliev,[9] K. E. Shestermanov,[22] S. S. Shimanskii,[9] V. S. Shvetcov,[10] G. Skoro,[9] N. Smirnov,[33] R. Snellings,[15] P. Sorensen,[6] J. Sowinski,[12] H. M. Spinka,[1] B. Srivastava,[23] E. J. Stephenson,[12] R. Stock,[11] A. Stolpovsky,[31] M. Strikhanov,[18] B. Stringfellow,[23] C. Struck,[11] A. A. P. Suaide,[31] E. Sugarbaker,[20] C. Suire,[2] M. Šumbera,[20] B. Surrow,[2] T. J. M. Symons,[15] A. Szanto de Toledo,[25] P. Szarwas,[29] A. Tai,[6] J. Takahashi,[25] A. H. Tang,[14] J. H. Thomas,[15] M. Thompson,[3] V. Tikhomirov,[18] M. Tokarev,[9] M. B. Tonjes,[17] T. A. Trainor,[30] S. Trentalange,[6] R. E. Tribble,[27] V. Trofimov,[18] O. Tsai,[6] T. Ullrich,[2] D. G. Underwood,[1] G. Van Buren,[2] A. M. VanderMolen,[17] I. M. Vasilevski,[10] A. N. Vasiliev,[22] S. E. Vigdor,[12] S. A. Voloshin,[31] F. Wang,[23] H. Ward,[28] J. W. Watson,[14] R. Wells,[20] G. D. Westfall,[17] C. WhittenJr.,[6] H. Wieman,[15] R. Willson,[20] S. W. Wissink,[12] R. Witt,[33] J. Wood,[6] N. Xu,[15] Z. Xu,[2] A. E. Yakutin,[22] E. Yamamoto,[15] J. Yang,[6] P. Yepes,[24] V. I. Yurevich,[9] Y. V. Zanevski,[9] I. Zborovský,[9] H. Zhang,[33] W. M. Zhang,[14] R. Zoulkarneev,[10] and A. N. Zubarev[9]

(STAR Collaboration)

[1]*Argonne National Laboratory, Argonne, Illinois 60439*
[2]*Brookhaven National Laboratory, Upton, New York 11973*
[3]*University of Birmingham, Birmingham, United Kingdom*
[4]*University of California, Berkeley, California 94720*
[5]*University of California, Davis, California 95616*
[6]*University of California, Los Angeles, California 90095*
[7]*Carnegie Mellon University, Pittsburgh, Pennsylvania 15213*
[8]*Creighton University, Omaha, Nebraska 68178*
[9]*Laboratory for High Energy (JINR), Dubna, Russia*
[10]*Particle Physics Laboratory (JINR), Dubna, Russia*
[11]*University of Frankfurt, Frankfurt, Germany*
[12]*Indiana University, Bloomington, Indiana 47408*
[13]*Institut de Recherches Subatomiques, Strasbourg, France*
[14]*Kent State University, Kent, Ohio 44242*

[15]*Lawrence Berkeley National Laboratory, Berkeley, California 94720*
[16]*Max-Planck-Institut fuer Physik, Munich, Germany*
[17]*Michigan State University, East Lansing, Michigan 48824*
[18]*Moscow Engineering Physics Institute, Moscow, Russia*
[19]*City College of New York, New York City, New York 10031*
[20]*Ohio State University, Columbus, Ohio 43210*
[21]*Pennsylvania State University, University Park, Pennsylvania 16802*
[22]*Institute of High Energy Physics, Protvino, Russia*
[23]*Purdue University, West Lafayette, Indiana 47907*
[24]*Rice University, Houston, Texas 77251*
[25]*Universidade de Sao Paulo, Sao Paulo, Brazil*
[26]*SUBATECH, Nantes, France*
[27]*Texas A & M, College Station, Texas 77843*
[28]*University of Texas, Austin, Texas 78712*
[29]*Warsaw University of Technology, Warsaw, Poland*
[30]*University of Washington, Seattle, Washington 98195*
[31]*Wayne State University, Detroit, Michigan 48201*
[32]*Institute of Particle Physics, CCNU (HZNU), Wuhan 430079 China*
[33]*Yale University, New Haven, Connecticut 06520*

Elliptic flow holds much promise for studying the early-time thermalization attained in ultrarelativistic nuclear collisions. Flow measurements also provide a means of distinguishing between hydrodynamic models and calculations which approach the low density (dilute gas) limit. Among the effects that can complicate the interpretation of elliptic flow measurements are azimuthal correlations that are unrelated to the reaction plane (nonflow correlations). Using data for Au + Au collisions at $\sqrt{s_{NN}} = 130$ GeV from the STAR time projection chamber, it is found that four-particle correlation analyses can reliably separate flow and nonflow correlation signals. The latter account for on average about 15% of the observed second-harmonic azimuthal correlation, with the largest relative contribution for the most peripheral and the most central collisions. The results are also corrected for the effect of flow variations within centrality bins. This effect is negligible for all but the most central bin, where the correction to the elliptic flow is about a factor of 2. A simple new method for two-particle flow analysis based on scalar products is described. An analysis based on the distribution of the magnitude of the flow vector is also described.

I. INTRODUCTION

In noncentral heavy-ion collisions, the initial spatial deformation due to geometry and the pressure developed early in the collision causes azimuthal momentum-space anisotropy, which is correlated with the reaction plane [1–4]. Measurements of this correlation, known as anisotropic transverse flow, provide insight into the evolution of the early stage of a relativistic heavy-ion collision [5]. Elliptic flow is characterized by the second-harmonic coefficient v_2 of an azimuthal Fourier decomposition of the momentum distribution [6–8], and has been observed and extensively studied in nuclear collisions from subrelativistic energies on up to RHIC. At top AGS and SPS energies, elliptic flow is inferred to be a relative enhancement of emission *in* the plane of the reaction. Elliptic flow is developed mostly in the first several femtometers/c (of the order of the size of nuclei) after the collision and thus provides information about the early-time thermalization achieved in the collisions [9]. Generally speaking, large values of flow are considered to be signatures of hydrodynamic behavior [6,10,11] although an alternative approach [12–16] is also argued to be consistent with the large elliptic flow for pions and protons at RHIC [17]. Models in which the colliding nuclei resemble interacting volumes of dilute gas—the low density limit [18] (LDL)—represent the limit of mean free path that is the opposite of hydrodynamics. It remains unclear to what extent the LDL picture can describe the data at RHIC, and valuable insights can be gained from mapping out the conditions under which hydrodynamic and LDL calculations can reproduce the measured elliptic flow.

Anisotropic flow refers to correlations in particle emission with respect to the reaction plane. The reaction plane orientation is not known in experiment, and anisotropic flow is usually reconstructed from the two-particle azimuthal correlations. But there are several possible sources of azimuthal correlations that are unrelated to the reaction plane—examples include correlations caused by resonance decays, (mini) jets, strings, quantum statistics effects, final state interactions (particularly Coulomb effects), momentum conservation, etc. The present study does not distinguish between the various effects in this overall category, but classifies their combined effect as "nonflow" correlations.

Conventional flow analyses are equivalent to averaging over correlation observables constructed from pairs of particles. When such analyses are applied to relativistic nuclear collisions where particle multiplicities can be as high as a

few thousand, the possible new information contained in multiplets higher than pairs remains untapped. A previous study of high-order flow effects focused on measuring the extent to which all fragments contribute to the observed flow signal [19], and amounted to an indirect means of separating flow and nonflow correlations. Given that flow analyses based on pair correlations are sensitive to both flow and nonflow effects, the present work investigates correlation observables constructed from particle quadruplets. The cumulant formalism removes the lower-order correlations which are present among any set of four particles, leaving only the effect from the so-called "pure" quadruplet correlation. The simplest cumulant approach, in terms of both concept and implementation, partitions observed events into four subevents. In the present study, the four-subevent approach is demonstrated, but our main focus is on a more elaborate cumulant method, developed by Borghini, Dinh, and Ollitrault [20,21]. There are indications that nonflow effects contribute at a negligible level to the four-particle cumulant correlation [20,21], making it unnecessary to continue to even higher orders for the purpose of separating the flow and nonflow signals. This observation is confirmed by our Monte Carlo simulations

In this analysis the observed multiplicity of charged particles within the detector acceptance is used to characterize centrality. This leads to some fluctuations of the impact parameter and, correspondingly, of the elliptic flow within each centrality bin, especially in the bin of highest multiplicity. In the present study, a correction is applied to reduce a possible bias in the measurements of the mean elliptic flow due to impact parameter fluctuations in the centrality bins to an insignificant level.

The present study begins with a review of the standard pair correlation method, and provides details concerning the approach adopted in earlier STAR publications [9,17] for treating nonflow correlations. A new method of pair flow analysis using the scalar product of flow vectors also is introduced. In the conventional method, a flow coefficient is calculated by the mean cosine of the difference in angle of two flow vectors. In the scalar product method, this quantity is weighted by the lengths of the vectors. The new method offers advantages, and is also simple to apply. Also, an analysis in terms of the distribution of the magnitude of the flow vector is discussed.

Measurements presented in this paper are based on Au+Au data at $\sqrt{s_{NN}}=130$ GeV recorded by STAR (Solenoidal Tracker at RHIC). A detailed description of the detector in its year-one configuration can be found elsewhere [22]. The main feature of the STAR time projection chamber (TPC) relevant to this analysis is its full azimuthal coverage (see Fig. 1). The analysis is based on 170 000 events corresponding to a minimum bias trigger. Events with a primary vertex beyond 1 cm radially from the beam or 75 cm longitudinally from the center of the TPC were excluded. Within the selected events, tracks were used for the estimation of the flow vector if all five of the following conditions were satisfied: they passed within 2 cm of the primary vertex, they had at least 15 space points in the TPC, the ratio of the number of space points to the expected maximum number of space
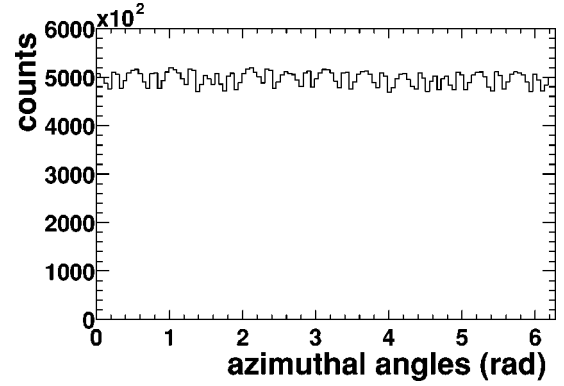

FIG. 1. The azimuthal angle distribution of tracks from minimum bias events. Dips are due to the reduced efficiency at sector boundaries of STAR TPC.

points was greater than 0.52, pseudorapidity $|\eta|<1.3$, and transverse momentum $0.1<p_t<2.0$ GeV/c. Particles over a wider range in η and p_t were correlated with this flow vector as shown in the graphs below. Centrality is characterized in eight bins of charged particle multiplicity, n_{ch}, divided by the maximum observed charged multiplicity, n_{max}, with a more stringent cut $|\eta|<0.75$ imposed only for this centrality determination. The above cuts are essentially the same as used in the previous STAR studies of elliptic flow [9,17].

II. TWO-PARTICLE CORRELATION METHODS

Anisotropic transverse flow manifests itself in the distribution of $\phi'=\phi-\Psi$, where ϕ is the measured azimuth for a track in detector coordinates, and Ψ is the azimuth of the estimated reaction plane in that event. The observed anisotropies are described by a Fourier expansion,

$$dN/d\phi' \propto 1 + 2v_{1,obs}\cos\phi' + 2v_{2,obs}\cos 2\phi' + \cdots . \quad (1)$$

Each measurable harmonic can yield an independent estimate Ψ_n of the event reaction plane via the event flow vector Q_n:

$$Q_n\cos n\Psi_n = \sum_i \cos n\phi_i,$$

$$Q_n\sin n\Psi_n = \sum_i \sin n\phi_i, \quad (2)$$

where the sums extend over all particles in a given event. The observed values of $v_{n,obs}$ corrected for the reaction plane resolution yield v_n [8]. Below we will also use the representation of the flow vector as a complex number with real and imaginary parts equal to x and y components defined in Eq. (2):

$$Q_n = \sum_i u_{n,i}, \quad (3)$$

where $u_{n,i}=e^{in\phi_i}$ is a unit vector associated with the ith particle; its complex conjugate is denoted by $u_{n,i}^*$.

A. Correlation between flow angles from different subevents: Estimate of nonflow effects

In order to report anisotropic flow measurements in a detector-independent form, it is customary to divide each event into two subevents and determine the resolution of the event plane by correlating the Q_n vector for the subevents [8,23]. In order to estimate the contribution from different nonflow effects one can use different ways of partitioning the entire event into two subevents. The partition according to particle charge should be more affected by resonance decay effects because the decay products of neutral resonances have opposite charge. The partition using two (pseudo) rapidity regions (better separated by $\Delta y \geq 0.1$) should greatly suppress the contribution from quantum statistics effects and Coulomb (final state) interactions.

Another important observation for the estimate of the nonflow effects is their dependence on centrality. The correlation between two subevent flow angles is

$$\langle \cos[2(\Psi_2^{(a)} - \Psi_2^{(b)})] \rangle \approx \left\langle \frac{\sum_{i=1}^{M_{sub}} u_i}{\sqrt{M_{sub}}} \cdot \frac{\sum_{j=1}^{M_{sub}} u_j^*}{\sqrt{M_{sub}}} \right\rangle$$
$$= \frac{M_{sub} M_{sub}}{M_{sub}} \langle u_i u_j^* \rangle \propto M_{sub}(v_2^2 + \delta_2),$$

$$(4)$$

where M_{sub} is the multiplicity of a subevent, and δ_2 denotes the nonflow contribution to two-particle correlations. For correlations due to small clusters, which are believed responsible for the dominant nonflow correlations [20], the strength of the correlation should scale in inverse proportion to the total multiplicity. Since the subevent multiplicity is proportional to the total multiplicity, we can define $\tilde{\delta}_2$ to be the multiplicity independent nonflow effect: $\delta_2 = \tilde{\delta}_2 / M_{sub}$. Collecting terms, we arrive at

$$\langle \cos[2(\Psi_2^{(a)} - \Psi_2^{(b)})] \rangle \propto M_{sub} v_2^2 + \tilde{\delta}_2. \tag{5}$$

What is important is that the nonflow contribution to $\langle \cos[2(\Psi_2^{(a)} - \Psi_2^{(b)})] \rangle$ is approximately independent of centrality. The typical shape of $\langle \cos[2(\Psi_2^{(a)} - \Psi_2^{(b)})] \rangle$ for flow (see, for example, Fig. 2) is peaked at midcentral events due to the fact that for peripheral collisions, M_{sub} is small, and for central events, v_2 is small. In the previous estimates [9,17] of the systematic errors, we have set the quantity $\tilde{\delta}_2 = 0.05$. The justification for this value was the observation of similar correlations for the first and higher harmonics (we have investigated up to the sixth harmonic). One could expect the nonflow contribution to be of a similar order of magnitude for all these harmonics, and HIJING [24] simulations support this conclusion. Given the value $\tilde{\delta}_2 = 0.05$, one simply estimates the contribution from nonflow effects to the measurement of v_2 from the plot of $\langle \cos[2(\Psi_2^{(a)} - \Psi_2^{(b)})] \rangle$ using Eq. (5).

Figure 2 shows the event plane correlation between two subevents, for each of the three different subevent partitions. In central events, it is seen that the correlation is stronger in
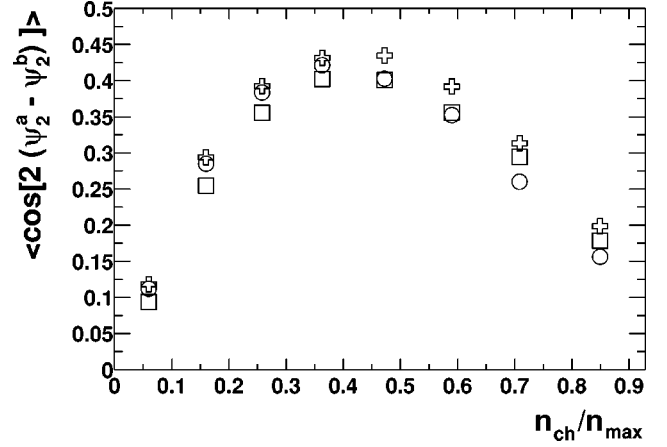

FIG. 2. Correlation between the event plane angles determined from pairs of subevents partitioned randomly (circles), partitioned with opposite signs of pseudorapidity (squares) and partitioned with opposite signs of charge (crosses). The correlation is plotted as a function of centrality, namely, charged particle multiplicity n_{ch} divided by the maximum observed charged multiplicity, n_{max}.

the case of subevents with opposite signs of charge compared to subevents partitioned randomly. This pattern might be due to resonance decays to two particles with opposite charges. The spread of the results for different subevent partitions is about 0.05, which is in accord with the number used for the estimates of the systematic errors.

The event plane resolution for full events is defined as $\langle \cos[n(\Psi_{measure} - \Psi_{true})] \rangle$, in which $\Psi_{measure}$ and Ψ_{true} are azimuthal angles for the measured reaction plane and the "true" reaction plane, respectively. The resolution with p_t weighting (see Sec. II B) can reach as high as 0.8, as shown in Fig. 3. The v_2 as a function of centrality is shown in Fig. 4, using different prescriptions to partition the particles into subevents. Again, partitioning into subevents with opposite sign of charge yields the highest elliptic flow signal, presumably because of neutral resonance (ρ^0, etc.) decay.
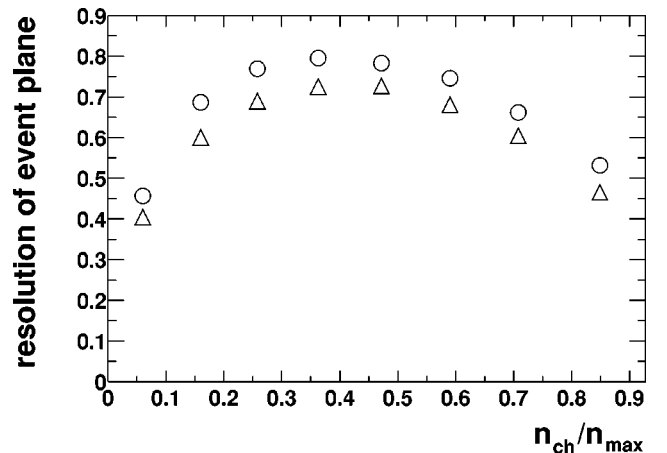

FIG. 3. The event plane resolution for full events as a function of centrality, using randomly partitioned subevents with (circles) and without (triangles) p_t weight.
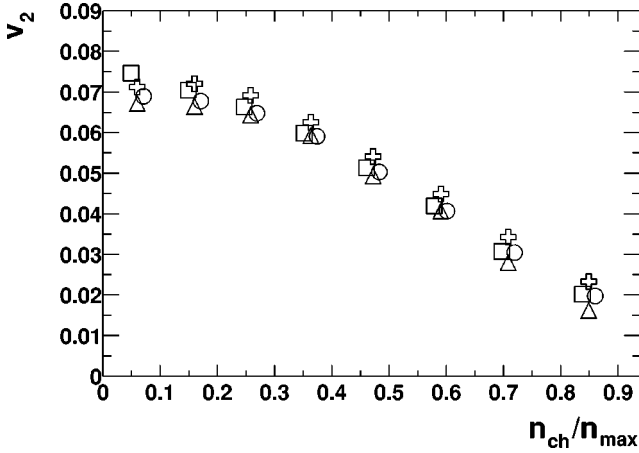
FIG. 4. Elliptic flow signal v_2 as a function of centrality, from study of the correlation between particle pairs consisting of randomly chosen particles (circles), particles with opposite signs of charge (crosses), particles with the same signs of charge (triangles), and particles with opposite signs of pseudorapidity (squares).

B. Weighting

If Eq. (3) is generalized to the form $Q_n = \Sigma_i w_i u_i$, where the w_i are weights adjusted to optimize the event plane resolution [8,25], then u_i should be replaced by $w_i u_i$ for all equations in this paper, and M should be replaced by $\Sigma_i w_i^2$ throughout Secs. II and IV B.

The best weight $w_i(\eta, p_t)$ is $v_2(\eta, p_t)$ itself [20]. In practice, since we know that v_2 is approximately proportional to p_t up to about 2 GeV/c, it is convenient to use p_t as the weight. It is found that p_t weighting can reduce the statistical error significantly, as demonstrated in Fig. 5.

C. Scalar product flow analysis

In a new scalar product method [26], each event is partitioned into two subevents, labeled by the superscripts a and b. The correlation between two subevents is

$$\langle Q_n^a Q_n^{b*} \rangle = \langle v_n^2 M^a M^b \rangle , \tag{6}$$

where M^a and M^b are the multiplicities for subevents a and b, respectively. The vectors Q_n^a and Q_n^b are constructed for the appropriate subevent as per Eq. (2).

Given the above, the flow relative to the true reaction plane can be readily calculated from unit momentum vectors $u_{n,i}(\eta, p_t)$ of the analyzed tracks by using Eq. (6) for the particle relative to the $2M$ other particles, and then dividing by the square root of Eq. (6) for the subevents. This gives

$$v_n(\eta, p_t) = \frac{\langle Q_n u_{n,i}^*(\eta, p_t) \rangle}{2 \sqrt{\langle Q_n^a Q_n^{b*} \rangle}} . \tag{7}$$

Autocorrelations are removed by subtracting particle i in the calculation of Q_n when taking the scalar product with $u_{n,i}$. This method weights events with the magnitude of the Q_n vector, and if Q_n is replaced by its unit vector, the above reduces to $\langle \cos n(\phi - \Psi) \rangle$, the conventional correlation method.
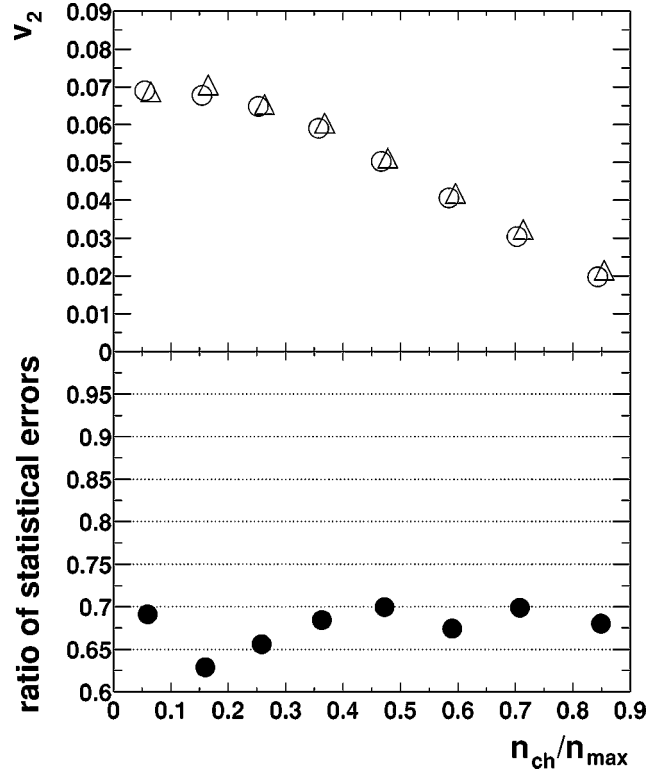

FIG. 5. The upper panel shows v_2 vs centrality using the conventional method, where the circles and triangles represent v_2 with and without p_t weighting, respectively. The statistical error is smaller than the symbol size. The lower panel shows the statistical error on v_2 with p_t weighting divided by the same without weighting.

Figure 6 demonstrates that the results from the scalar product method are indeed very close to those of the conventional method. In this calculation, the subevents are generated by random partitioning. However, the detailed comparison of two results reveals a small systematic difference. The difference might have origin in the approximations (the central limit theorem) used in the conventional method and that are not required in the scalar product method. In addition, the scalar product method has the benefit of smaller statistical errors and is very simple to implement.

III. DISTRIBUTION IN THE MAGNITUDE OF THE FLOW VECTOR

In this section we study elliptic flow by the analysis of the distribution in the magnitude of the flow vector. The method was used by the E877 Collaboration at the AGS for the first observation of anisotropic flow at ultrarelativistic nuclear collisions [27]. This method is based on the observation that anisotropic flow strongly modifies the distribution of the magnitude of the flow vector [7,8,20,28]. Very strong flow leads to the distribution $dP/(Q_n dQ_n)$ with a local minimum at $Q = 0$, which reflects the fact that for the case of strong flow all particle momentum unit vectors are aligned in the flow direction. On the other hand, the nonflow effects, two-, and few-particle azimuthal correlations lead to an increase in
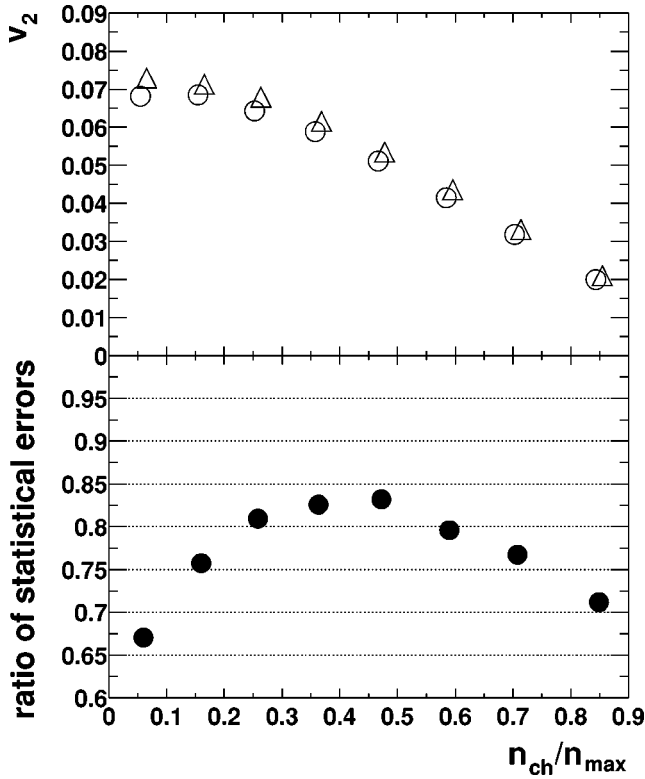
FIG. 6. The upper panel presents v_2 vs centrality from the scalar product method (triangles) and the conventional random subevent method (circles). All statistical errors are smaller than the symbol size. The statistical error for the scalar product method divided by that for the conventional method is shown in the lower panel.

FIG. 7. Reduced flow vector distributions for centrality bin 5 plotted in two ways. Solid lines correspond to the fit with two parameters, v_2 and g_2, and dashed lines correspond to the fit assuming zero real flow.

the statistical fluctuation width of the distribution. The effect can be understood by considering the flow vector composed of many clusters but randomly distributed in the azimuthal space. In the limit of large multiplicity and neglecting the contribution from higher harmonics (for a more accurate consideration, see Refs. [20,26,29]) the distribution can be described by [7,8,28]

$$\frac{dP}{q_n dq_n} = \frac{1}{\sigma_n^2} \exp\left(-\frac{v_n^2 M + q_n^2}{2\sigma_n^2}\right) I_0\left(\frac{q_n v_n \sqrt{M}}{\sigma_n^2}\right), \quad (8)$$

where I_0 is the modified Bessel function. We have introduced the variable $q_n = Q_n/\sqrt{M}$, which greatly reduces the effect on the shape of the distribution from averaging over events with different multiplicities. In a more general case using weights, one should use $q_n = Q_n/(\sqrt{M \langle w_i^2 \rangle})$. In this way the width of the q distribution is independent of multiplicity:

$$\sigma_n^2 = 0.5(1 + g_n), \quad (9)$$

with g_n reflecting the change in the width of the distribution due to nonflow effects (and to some extent to the averaging over events with different multiplicities).

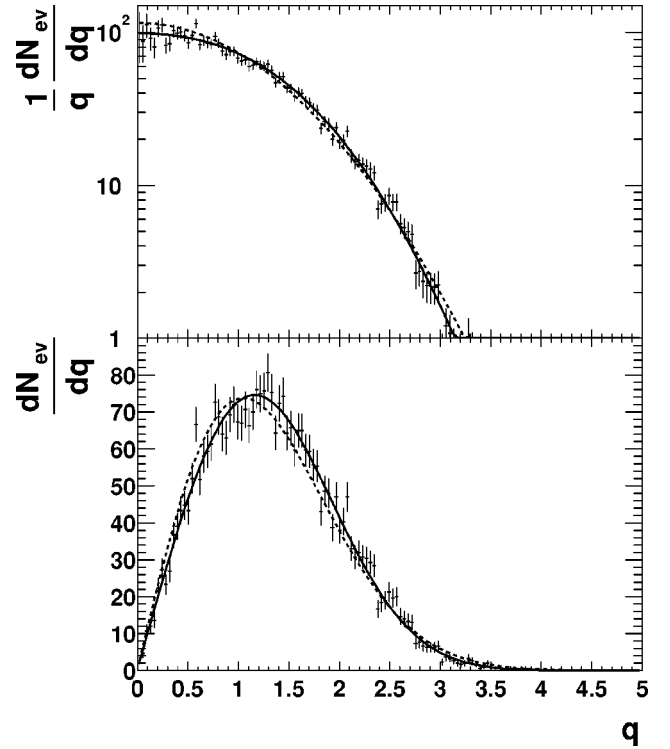We have fitted distributions of q_2, the second-harmonic reduced flow vector, in two different ways. First, the distributions in all different centrality bins have been fitted with two independent parameters, v_2 and g_2. The nonflow contribution parameter g_2 has been found to be in the range of 0.18–0.32 for all centralities except the most peripheral one. One should not expect a good fit for the most peripheral bin, for it is a mixture of events in a wide multiplicity range from 20 to 100. Better fit results for this bin could be achieved if the bin would be split into several sub-bins with smaller relative multiplicity variations. The relative multiplicity variation in the other bins is much smaller. The q distribution for the centrality bin 5 is presented in Fig. 7. The two fit functions correspond to the case of a fit with two parameters, v_2 and g_2, and to the case of a one-parameter fit of g_2 for $v_2 = 0$. Note that the dashed curves are systematically higher or lower than the data points in different q regions. In the lower part of Fig. 7 one can see that the anisotropic flow pushes the q distribution out to larger values. If the flow were great enough one could select events based on the q values.

In the second method we fit q distributions in centrality bins 2–8 simultaneously with different v_2 values for each centrality bin but the same value of g. (This assumption is similar to the assumption of $\tilde{\delta} = \text{const}$ in the preceding section. See also the discussion in Refs. [8,20,28]). We find $g = 0.29 \pm 0.02$. The results of the fits are presented in Fig. 8. The deviation from the standard method results are due to the nonflow contributions.
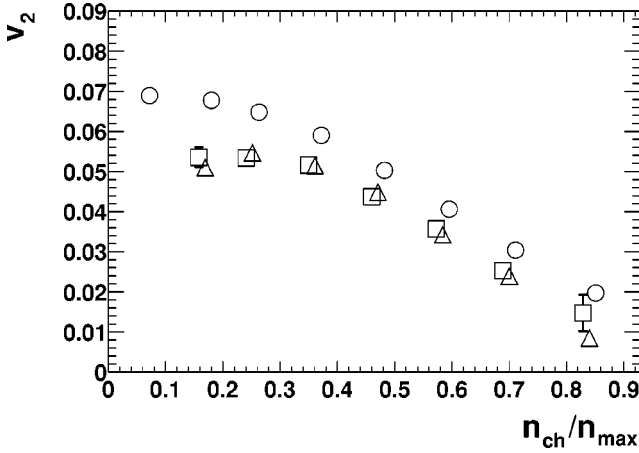
FIG. 8. Elliptic flow as determined from the fits to the q distributions in different centrality bins. The circles are from the standard method with random subevents. For the squares, all the centralities were fit separately. For the triangles, centrality bins 2–8 were fit with the same value of the nonflow parameter.

IV. FOUR-PARTICLE CORRELATIONS

A. Motivation for cumulants

In experiments, it is necessary to rely on correlations between particles to determine the event plane since the reaction plane is not a direct observable. The assumption underlying conventional pair correlation analyses (including the scalar product method discussed in Sec. II C above) is that nonflow correlations of the type mentioned in Sec. I are negligible compared to the flow, or at most, are comparable to other systematic uncertainties. In past studies [8,30,31], nonflow correlations have been discussed with specific reference to their origin, such as momentum conservation, Bose-Einstein correlations, Coulomb effect, jets, resonance decays, etc. In the first two studies of elliptic flow in STAR [9,17], the nonflow effect from jets and resonances was estimated using the approach explained in Sec. II A above, and this established an upper limit on the nonflow contribution to the reported v_2 signal. This limit played a role in determining the systematic error on the published measurements.

Anisotropic flow is a genuine multiparticle phenomenon, which justifies the use of the term *collective flow*. It means that if one considers many-particle correlations instead of just two-particle correlations, the relative contribution of nonflow effects (due to few-particle clusters) should decrease. Considering many-particle correlations, one has to subtract the contribution from correlations due to lower-order multiplets. Formally, one should use cumulants [21,32–34] instead of simple correlation functions. Let us explain this with an example for four-particle correlations. The correlation between two particles is

$$\langle u_{n,1}u_{n,2}^* \rangle \equiv \langle e^{in\phi_1}e^{-in\phi_2} \rangle = v_n^2 + \delta_n, \qquad (10)$$

where n is the harmonic, and the average is taken over all pairs of particles in a given rapidity and transverse momentum region, and over all events in an event sample. The δ_n

represents the contribution to the pair correlation from nonflow effects. Correlating four particles, one gets

$$\langle u_{n,1}u_{n,2}u_{n,3}^*u_{n,4}^* \rangle = v_n^4 + (2 \times 2)v_n^2\delta_n + 2\delta_n^2. \qquad (11)$$

In this expression, two factors of 2 in front of the middle term correspond to the two ways of pairing (1,3)(2,4) and (1,4)(2,3) and account for the possibility to have nonflow effects in the first pair and flow correlations in the second pair and vice versa. The factor 2 in front of the last term is due to the two ways of pairing. The pure four-particle nonflow correlation is omitted from this expression—see the discussion below about the possible magnitude of such a contribution. What is remarkable is that if one subtracts from the expression (11) twice the square of the expression (10), one is left with only the flow contributions

$$\langle\langle u_{n,1}u_{n,2}u_{n,3}^*u_{n,4}^* \rangle\rangle \equiv \langle u_{n,1}u_{n,2}u_{n,3}^*u_{n,4}^* \rangle - 2\langle u_{n,1}u_{n,2}^* \rangle^2 = -v_n^4, \qquad (12)$$

where the notation $\langle\langle \cdots \rangle\rangle$ is used for the *cumulant*. The cumulant of order two is just $\langle\langle u_{n,1}u_{n,2}^* \rangle\rangle = \langle u_{n,1}u_{n,2}^* \rangle$.

In flow analysis, one is interested not only in the so-called global flow values, but also in differential flow as a function of rapidity and transverse momentum. In a four-particle correlation approach, this can also be done in a similar manner, now correlating a particle, for example, in a particular p_t bin, with three particles from a common "pool." Assuming that the particle b is that from a particular bin, one gets for a differential flow study,

$$\langle u_{n,b}u_{n,1}^* \rangle = v_{n;b}v_n + \delta_{n;b}, \qquad (13)$$

where we have introduced the notation $v_{n;b}$ for the flow value corresponding to the bin under study, and $\delta_{n;b}$ for the corresponding nonflow contribution. Then for the correlation with three particles from the pool,

$$\langle u_{n,b}u_{n,1}u_{n,2}^*u_{n,3}^* \rangle = v_{n;b}v_n^3 + 2v_n^2\delta_{n;b} + 2v_nv_{n;b}\delta_n + 2\delta_n\delta_{n;b}. \qquad (14)$$

In this case, in order to remove the nonflow contribution, one has to subtract from Eq. (14) twice the product of expressions (10) and (13),

$$\langle u_{n,b}u_{n,1}u_{n,2}^*u_{n,3}^* \rangle - 2\langle u_{n,b}u_{n,1}^* \rangle\langle u_{n,1}u_{n,2}^* \rangle = -v_n^3v_{n;b}. \qquad (15)$$

Assuming that the average flow value for the particles in the pool is known, one gets the desired differential flow value for the particular bin under study.

In Eq. (11), we have neglected the contribution from the pure four-particle correlations due to nonflow effects. Let us now estimate the upper limit for such a contribution. Assume that *all* particles are produced via four-particle clusters. All daughters of the decay of such a cluster could, in principle, be within one to two units of rapidity from each other. Then the contribution would be

$$6f/M^3, \qquad (16)$$

where M is the *total* multiplicity within those one to two units of rapidity, and f is $\langle[\cos 2(\phi_1-\phi_2)]^2\rangle$, averaged over all cluster decay products. Assuming a perfect alignment, $f = 1$, and multiplicity $M = 1000$, this would give us a possible error in v_2 measurements of the order of

$$\delta v \sim (v_2^4 + 6/1000^3)^{1/4} - v_2. \tag{17}$$

This would give only a 3% relative error on the v_2 signal of 0.015, and would drop very rapidly with increasing real v_2 signal. This calculation is for the case of 100% of the particle production via four-particle clusters and a perfect alignment of decay products. A more realistic scenario would give a much smaller estimate.

B. Four-subevent method

In order to apply the four-particle correlation approach to the analysis of real data, one should perform an average over all possible quadruplets of particles in a given event. Bearing in mind that the average multiplicity in a central STAR event is well beyond 1000, it becomes a nontrivial task. The simplest solution to the problem is the four-subevent method where one partitions all tracks (for example, randomly) into four groups (subevents) and calculates a flow vector for each of the groups,

$$Q_n = \sum_i u_{n,i}, \tag{18}$$

where the sum is over all particles in the group. Using these subevents, the problem becomes much simpler computationally. For example,

$$\langle u_{n,1} u_{n,2} u_{n,3}^* u_{n,4}^* \rangle = \langle Q_{n,1} Q_{n,2} Q_{n,3}^* Q_{n,4}^* / (M_1 M_2 M_3 M_4) \rangle, \tag{19}$$

where M_i are the corresponding subevent multiplicities. The cumulant calculation is straightforward:

$$\langle\langle u_{n,1} u_{n,2} u_{n,3}^* u_{n,4}^* \rangle\rangle = \left\langle \frac{Q_{n,1} Q_{n,2} Q_{n,3}^* Q_{n,4}^*}{M_1 M_2 M_3 M_4} \right\rangle$$
$$- 2[\langle Q_{n,1} Q_{n,2}^* / (M_1 M_2) \rangle]^2. \tag{20}$$

The four-subevent method is very simple, both in logic and in implementation. The price for these benefits is lower statistical power, because the method does not take into account all possible quadruplets. Some improvement could be reached by splitting the event into more than four subevents and correlating all possible combinations of four. In the analysis of the STAR data we use eight subevents. A more general cumulant formalism, based on the cumulant generating function [21,31] offers advantages for a four-particle analysis in the context of the present limited sample size.

C. Cumulant generating function

The cumulant generating function approach offers a formal and convenient way to study flow and nonflow contri-

butions systematically. Following the method of Ref. [21], the cumulant to order four is defined by

$$\langle\langle u_1 u_2 u_3^* u_4^* \rangle\rangle \equiv \langle u_1 u_2 u_3^* u_4^* \rangle - \langle u_1 u_3^* \rangle \langle u_2 u_4^* \rangle$$
$$- \langle u_1 u_4^* \rangle \langle u_2 u_3^* \rangle, \tag{21}$$

where, as above, the double angle bracket notation represents the cumulant expression shown explicitly on the right-hand side. The subscript for the harmonic order, n, has been dropped. The cumulant $\langle\langle u_1 u_2 u_3^* u_4^* \rangle\rangle$ involves only pure four-particle correlations, since the two-particle only correlations among the quadruplets have been explicitly subtracted away.

In the presence of flow, the cumulant becomes

$$\langle\langle u_1 u_2 u_3^* u_4^* \rangle\rangle = -v_n^4 + O\left(\frac{1}{M^3} + \frac{v_{2n}^2}{M^2}\right), \tag{22}$$

where M is the multiplicity of the events, the term of order $1/M^3$ represents the remaining four-particle nonflow effects, and the term of order v_{2n}^2/M^2 is the contribution of the $2n$ higher harmonic. The cumulant to higher orders and the corresponding generalization has also been determined [21]. Likewise, the cumulant of order two reduces to the equivalent of a pair correlation analysis of the conventional type. Statistical uncertainties associated with a cumulant analysis increase with increasing order from two to four.

The definition of the cumulant is simple, but it is tedious to calculate the moments term-by-term on the right-hand side of Eq. (21). Fortunately, the cumulant can be computed more easily from the generating function [21]

$$G_n(z) = \prod_{j=1}^M \left(1 + \frac{z^* u_j + z u_j^*}{M}\right), \tag{23}$$

where $z \equiv |z| e^{i\alpha}$ is an arbitrary complex number, z^* denotes its complex conjugate. The generating function itself has no direct physical meaning, but the coefficients of the expansion of $\langle G_n \rangle$ in powers of z, z^* yield the correlations of interest:

$$\langle G_n \rangle = 1 + \left\langle \frac{M-1}{M} \right\rangle |z|^2 \langle u_1 u_2^* \rangle$$
$$+ \left\langle \frac{(M-1)(M-2)(M-3)}{4M^3} \right\rangle |z|^4 \langle u_1 u_2 u_3^* u_4^* \rangle$$
$$+ \cdots. \tag{24}$$

One can use these correlations to construct the cumulants. In the limit of large M, $\langle G_n \rangle$ can be used to obtain the cumulant generating function directly:

$$M[\langle G_n(z) \rangle^{1/M} - 1] = \sum_k \frac{|z|^{2k}}{(k!)^2} \langle\langle u_1 \cdots u_k u_{k+1}^* \cdots u_{2k}^* \rangle\rangle. \tag{25}$$

The left-hand side of Eq. (25) is what is measured, and in order to extract the cumulants on the right, k equations of the

form of Eq. (25) are needed to solve for k undetermined parameters. This can be accomplished by repeating the process with k different values of $|z|$. It is found that suggested magnitudes of $|z|$ in Ref. [21], namely, $r_0 \sqrt{p}$ with $r_0 = 1.5$ and $p = 1, \ldots, k$, are fairly good, since results from optimized values [35] of r_0 show almost no difference. Results in this paper are by default calculated with $r_0 = 1.5$. Since M fluctuates from one event to the other, for events within a multiplicity bin, we use the average value $\langle M \rangle$ in Eq. (25) instead of M.

For experimental analysis, it is sufficient to take the first three terms in Eq. (25). Once the cumulant has been computed, extracting the integrated flow value is straightforward because, for instance, $v_n^4 = -\langle\langle u_1 u_2 u_3^* u_4^* \rangle\rangle$.

When a nonunit weight is used, the integrated flow value described above becomes $\langle w \cos n\phi' \rangle$, which is not exactly v_n but an approximation. However, the differential flow can be calculated exactly (see below) no matter what weight is used. The integrated flow with nonunit weight can be obtained by integrating the differential flow. All integrated flow results in this paper (except for results from the four-subevent method) are obtained by integrating over the differential flow.

For differential flow (flow in a bin of η and/or p_t), Eq. (25) is replaced by

$$\frac{\langle u_d G_n(z) \rangle}{\langle G_n(z) \rangle} \equiv \sum_{k,l} \frac{z^{*k} z^l}{k! \, l!} \langle\langle u_d u_1 \cdots u_k u_{k+1}^* \cdots u_{k+l}^* \rangle\rangle. \tag{26}$$

where u_d is the unit vector for a particle in the selected bin. Following a similar procedure as in the case of the integrated flow, the cumulant $\langle\langle u_d u_1 u_2^* u_3^* \rangle\rangle$ is computed, but it now contains the angle of the particular particle of interest and three other particles from the pool. Then the differential flow is [21]

$$v_n = -\frac{\langle\langle u_d u_1 u_2^* u_3^* \rangle\rangle}{(-\langle\langle u_1 u_2 u_3^* u_4^* \rangle\rangle)^{3/4}}. \tag{27}$$

Equation (27) is for unit weight. It can be easily generalized for nonunit weight, and the formula still holds.

Some detectors have substantial asymmetry in their response as a function of the azimuth in detector coordinates, in which case it is necessary to prevent distortion of the measured flow signals by employing one of two possible compensation methods [8]—applying a shifting transformation which recenters Q: $\langle Q_n \sin n\Psi_n \rangle = 0$ and $\langle Q_n \cos n\Psi_n \rangle = 0$ [see Eq. (2)], or applying weighting factors to force a flat Ψ distribution. In the present study, no noticeable difference is observed with and without explicit compensation for detector asymmetry, as expected in light of the excellent azimuthal symmetry of the STAR TPC. All plots in this paper are made without compensation for detector asymmetry. However, it should be noted that cumulants, as defined by the generating function, also correct for small anisotropies in the detector acceptance. For instance, the cumulant

$$\langle\langle u_1 u_2^* \rangle\rangle = \langle u_1 u_2^* \rangle - \langle u_1 \rangle \langle u_2^* \rangle \tag{28}$$
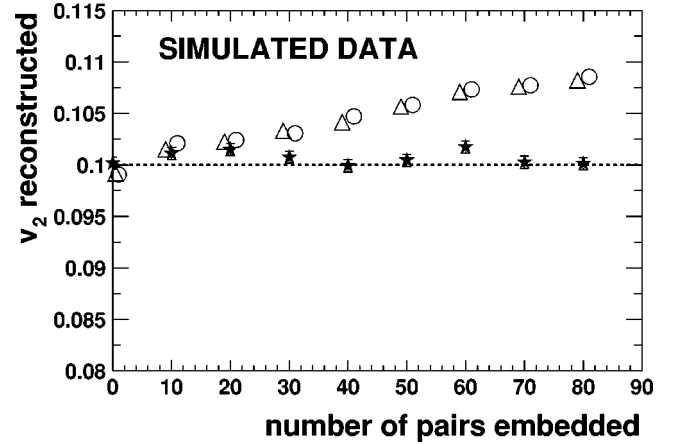

FIG. 9. Reconstructed v_2 from the conventional method (circles), from the second-order cumulant method (triangles), and from the fourth-order cumulant method (stars), for simulated events as a function of the number of embedded back-to-back track pairs. The horizontal dashed line marks the level of the true elliptic flow $v_2 = 0.10$, as imposed on the simulated events, including the back-to-back track pairs. The statistical error is smaller than the symbol size. The multiplicity for all events is 500.

amounts to an implementation of the shifting compensation method mentioned above.

D. Simulations

In order to test the cumulant method as well as the analysis procedure, the MEVSIM [36] event generator has been used to make events with various mixtures of flow and nonflow effects. In all cases, the number of simulated events in a data set is $20k$, and the multiplicity is 500. Figure 9 shows one such set of simulations. Nine datasets with $v_2 = 0.10$ were produced, then a simple nonflow effect consisting of embedded back-to-back track pairs was introduced at various levels, ranging from zero up to 80 pairs per simulated event. These pairs simulate resonances that decay to two daughters with a large energy release. In Fig. 9, we consider the scenario where the embedded pairs themselves are correlated with the event plane with the same $v_2 = 0.10$. Figure 9 shows that the fourth-order cumulant v_2 always reconstructs the expected 10% v_2, while the v_2 from the pair correlation analysis methods can only recover the correct input if nonflow pairs are not embedded.

If back-to-back pairs are instead randomly distributed in the azimuth, the true flow should decrease and the expected variation can be computed as the number of random tracks are known. Figure 10 shows such a simulation, and again it is found that only the fourth-order cumulant v_2 agrees with the expected elliptic flow, while the inferred v_2 based on pair correlation analyses is distorted in the presence of the simulated nonflow effects. The role of resonances produced in real collisions may be closer to one or the other of the above two simulated scenarios, but in either case, the nonflow effect is removed by the fourth-order cumulant analysis.

In Fig. 11, consideration is given to the possible effect of resonances which decay with smaller energy release, having
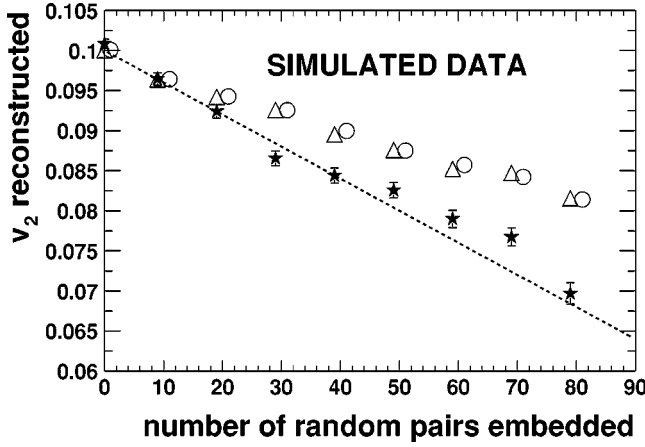
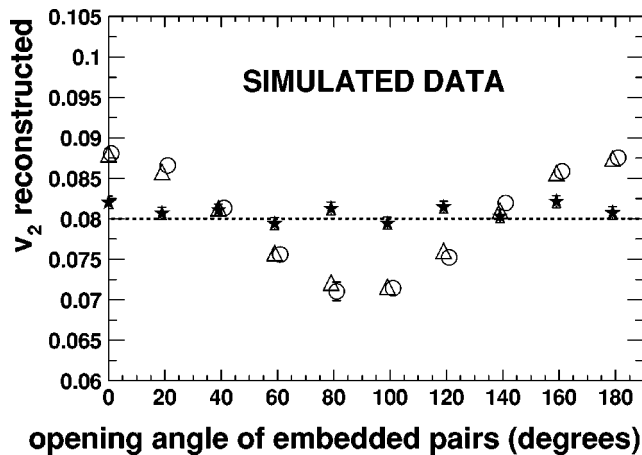FIG. 10. Reconstructed v_2 from the conventional method (circles), from the second-order cumulant method (triangles), and from the fourth-order cumulant method (stars), for simulated events as a function of the number of embedded back-to-back track pairs. Unlike in the previous figure, the embedded back-to-back pairs are randomly distributed relative to the event plane, and so the true resultant v_2, indicated by the dashed line, decreases as more pairs are embedded. The multiplicity for all events is 500.
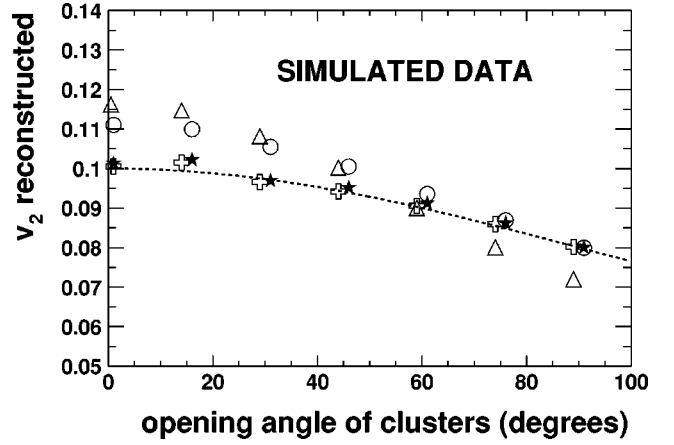

FIG. 12. Elliptic flow from the conventional method (circles), and from the second-order (triangles), fourth-order (stars), and sixth-order (crosses) cumulant methods. This is for simulated events as a function of azimuthal angle between two back-to-back track pairs. The dashed line marks the level of the true elliptic flow.

an azimuthal opening angle Φ in the laboratory. The simulated events were generated with an imposed flow $v_2 = 0.08$, while in each event, 50 pairs with the same Φ were embedded, each such pair having a random orientation relative to the event plane. Ten data sets were produced, with Φ (the abscissa in Fig. 11) varying in 20° steps between zero and 180°. Again, only the fourth-order cumulant v_2 (stars) recovers the true elliptic flow signal.

In order to test how the various methods respond to nonflow correlations associated with four-particle clusters, the simulated events in Fig. 12 were generated with an imposed flow $v_2 = 0.10$, after which 25 four-particle clusters were em-

bedded in each event. Each cluster consists of two back-to-back pairs with an azimuthal opening angle Φ between them. Seven data sets were produced, with Φ (the abscissa in Fig. 12) varying in 15° steps between zero and 90°. The clusters were oriented such that a track bisecting Φ would contribute to the overall flow with $v_2 = 0.10$. The fourth-order cumulant (stars) and the sixth-order cumulant (crosses) both reconstruct the true elliptic flow (dotted line). Note that the four-particle correlation introduced by the clusters is $1/M^2$ times the pair correlation part, resulting in little difference between v_2 from the fourth- and sixth-order cumulant methods. This result further illustrates the point (see also the end of Sec. III A) that nonflow effects are believed to contribute at a negligible level to the four-particle correlation, and for this
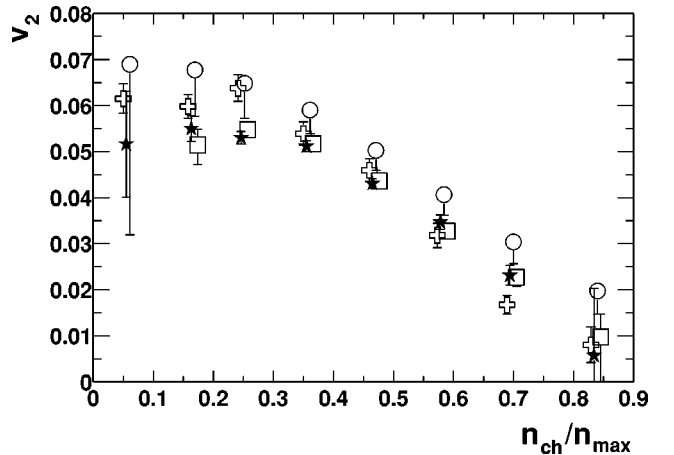

FIG. 11. Elliptic flow from the conventional method (circles), from the second-order cumulant method (triangles), and from the fourth-order cumulant method (stars), for simulated events as a function of azimuthal angle between the two tracks in each of 50 embedded pairs per event, with the 50 pairs each having a random orientation relative to the event plane. The horizontal dashed line marks the level of the true elliptic flow $v_2 = 0.08$.

FIG. 13. Measured elliptic flow vs centrality for Au+Au at $\sqrt{s_{NN}} = 130$ GeV. The circles show the conventional v_2 with estimated systematic uncertainty due to nonflow [37], the stars show the fourth-order cumulant v_2 from the generating function, the crosses show the conventional v_2 from quarter events, and the squares show the fourth-order cumulant v_2 from the four-subevent method.
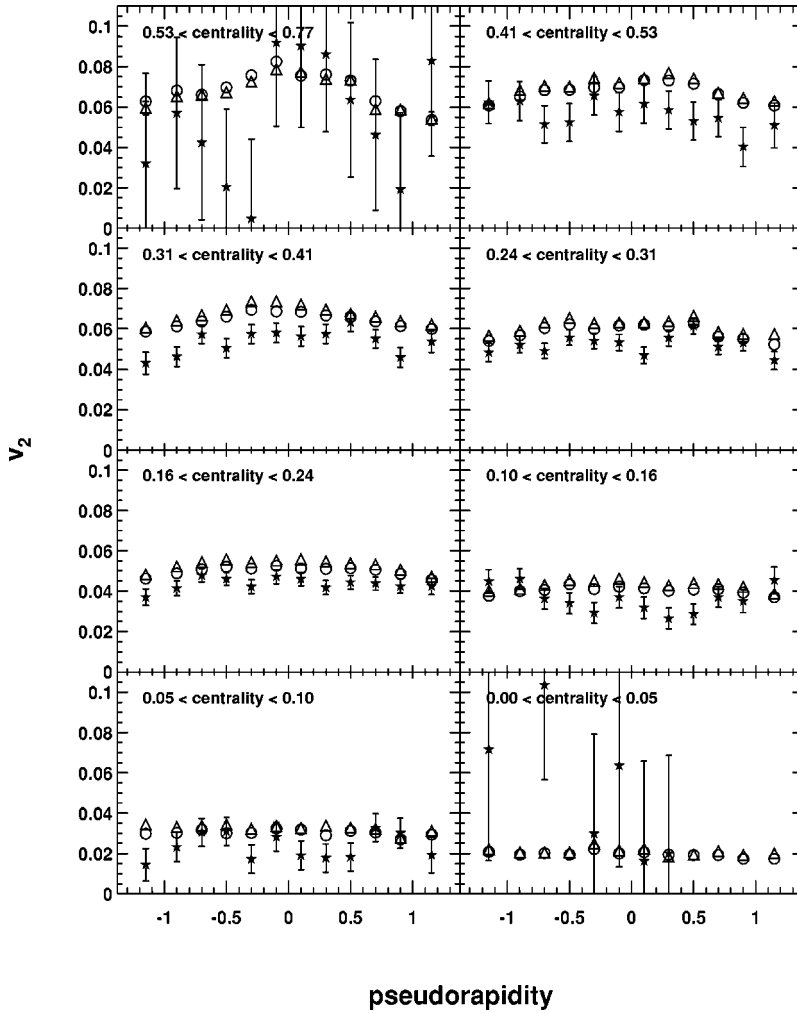
FIG. 14. Reconstructed v_2 vs pseudorapidity from the conventional method (circles), from the second-order cumulant method (triangles), and from the fourth-order cumulant method (stars), in eight centrality bins. The upper left panel shows the most peripheral events, and the lower right the most central.

reason, there may be little advantage in extending cumulant analyses to orders higher than four.

E. Results from STAR

Figure 13 shows measured elliptic flow versus centrality, where the latter is characterized by charged particle multiplicity n_{ch} divided by the maximum observed charged particle multiplicity, n_{max}. The conventional v_2 (circles), the fourth-order cumulant v_2 from the generating function (stars), and the fourth-order cumulant v_2 from the four-subevent method (squares) are compared. The cross symbols in Fig. 13 represent the conventional v_2 signal for the case where each observed event is partitioned into four quarter events, which are then analyzed like independent events. All tracks in each quarter event have the same sign of charge and the same sign of pseudorapidity. Furthermore, the event plane for quarter events is constructed using only tracks with $p_t < 0.5$ GeV/c, which serves to minimize the influence of nonflow associated with high-p_t particles. It is clear that the nonflow effect is present at all centralities, and its relative magnitude is least at intermediate multiplicities.

Figure 14 shows v_2 as a function of pseudorapidity and Fig. 15 shows v_2 as a function of transverse momentum. The eight panels correspond to the eight bins of relative multi-plicity in Fig. 13 but the centrality is now defined in terms of the total geometric cross section (see first three columns of Table I). These results illustrate the main disadvantage of the higher-order cumulant approach compared with any of the two-particle methods, namely, larger statistical errors, and this can be seen to be a serious shortcoming in cases where simultaneous binning in several variables results in small sample sizes. However, Fig. 13 demonstrates that, especially for the more peripheral bins, the statistical uncertainties for the fourth-order cumulant method are smaller than the systematic uncertainties for the two-particle methods.

Figures 16 and 17 are again plots of elliptic flow versus pseudorapidity and versus transverse momentum, respectively. Here the v_2 is integrated over centrality bins 2–7. Bins 1 and 8 are not included in this average, otherwise they would significantly increase the statistical error on the result. The fourth-order cumulant v_2 is systematically about 15% lower than the conventional pair and cumulant pair calculations, indicating that nonflow effects contribute to v_2 analyses of the latter kind. The v_2 signal based on quarter events (as defined in the discussion of Fig. 13) is closer to the fourth-order cumulant, although still larger on average, implying that this pair analysis prescription is effective in removing some, but not all, nonflow effects.
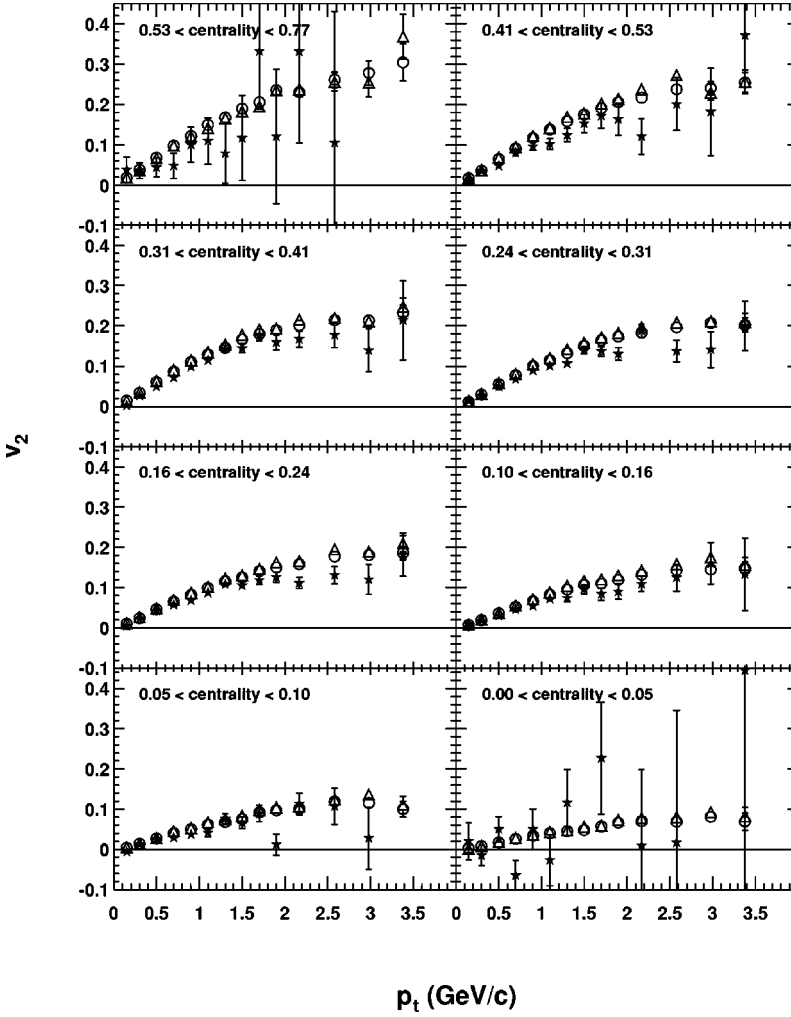
FIG. 15. Reconstructed v_2 vs p_t from the conventional method (circles), from the second-order cumulant method (triangles), and from the fourth-order cumulant method (stars), in eight centrality bins. The upper left panel shows the most peripheral events, and the lower right the most central.

Figure 17 verifies that the $v_2(p_t)$ curve flattens above 2 GeV/c [37]. There is theoretical interest in the question of whether or not $v_2(p_t)$ continues flat at higher p_t or eventually goes down [38]—this issue is the subject of a separate analysis [39], and the statistics of year-one data from STAR is not suited for addressing this question via a four-particle cumulant analysis.

Figure 18 presents the p_t dependence of the correction factor for nonflow. Within errors, the relative nonflow effect is seen to be about the same or increasing very weakly from low p_t through $p_t \sim 4$ GeV/c—a somewhat surprising result, given the presumption that the processes responsible for nonflow are different at low and high p_t. Figure 19, which presents v_2 from quarter-events divided by the conventional v_2, both based on event planes constructed from particles with $p_t < 0.5$ GeV/c, offers a useful insight regarding the approximate p_t independence of nonflow. This ratio roughly characterizes the contribution to nonflow from resonance decays

TABLE I. Tabulated values of observed charged particle multiplicity, n_{ch}/n_{max}, centrality in percentages of total geometric cross section, impact parameter with spread (root mean square) inferred from HIJING, the initial spatial anisotropy ε, and the final corrected elliptic flow based on fourth-order cumulants.

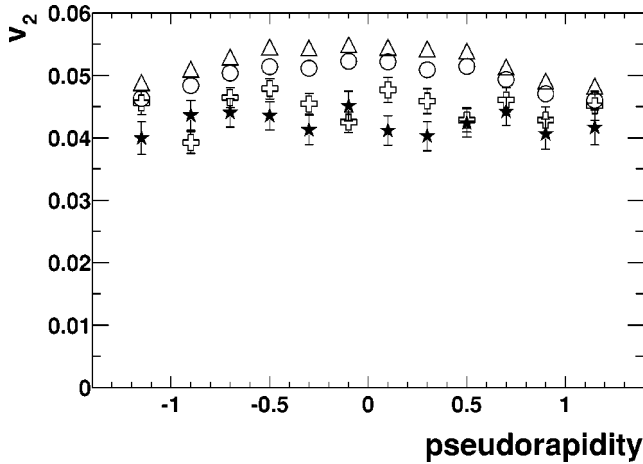| $\langle n_{ch}\rangle$	$\langle n_{ch}/n_{max}\rangle$	cross section	$\langle b\rangle$ (fm)	rms (b)	$\langle\varepsilon\rangle$	$\langle v_2\rangle$
53^{47}_{33}	0.060	53–77 %	12.23	0.99	0.420	0.052 ± 0.012
140^{40}_{40}	0.160	41–53 %	10.36	0.70	0.415	0.055 ± 0.003
227^{43}_{47}	0.258	31–41 %	9.06	0.68	0.371	0.053 ± 0.001
319^{41}_{49}	0.363	24–31 %	7.91	0.64	0.319	0.051 ± 0.001
415^{45}_{55}	0.472	16–24 %	6.80	0.70	0.261	0.043 ± 0.001
519^{41}_{59}	0.590	10–16 %	5.56	0.72	0.197	0.035 ± 0.002
622^{38}_{62}	0.708	5–10 %	4.26	0.80	0.131	0.023 ± 0.002
746^{124}_{86}	0.849	Top 5%	2.53	1.00	0.058	0.012 ± 0.015

FIG. 16. Elliptic flow vs pseudorapidity from the conventional method (circles), from the second-order cumulant method (triangles), from quarter events (crosses), and from the fourth-order cumulant method (stars), averaged over all centralities from bin 2–7, as defined in Figs. 14 and 15.

and from other sources that primarily affect v_2 at lower p_t, whereas nonflow from (mini) jets ought to be about equally present in the numerator and the denominator of the ordinate in Fig. 19. A comparison of Figs. 18 and 19 accordingly does not contradict the implicit assumption that different phenomena dominate nonflow in different p_t regions, and implies that the total resultant nonflow correction by coincidence happens to be roughly the same throughout the p_t range under study.

Following the approach of Sec. II B, the options of weighting each track by either unity or p_t have been compared in the fourth-order cumulant analysis. Figure 20 demonstrates that the STAR results are consistent in the two cases, and the p_t weighting yields smaller statistical errors. All STAR results presented in this paper are computed with p_t weighting unless otherwise stated.
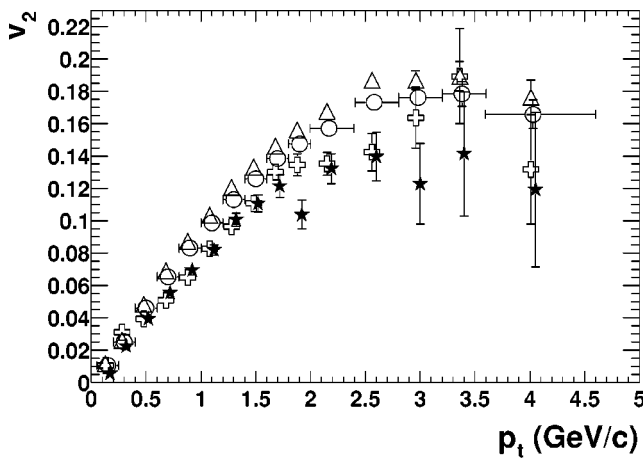

FIG. 17. Elliptic flow vs transverse momentum from the conventional method (circles), from the second-order cumulant method (triangles), from quarter events (crosses), and from the fourth-order cumulant method (stars), averaged over all centralities from bin 2–7, as defined in Figs. 14 and 15.
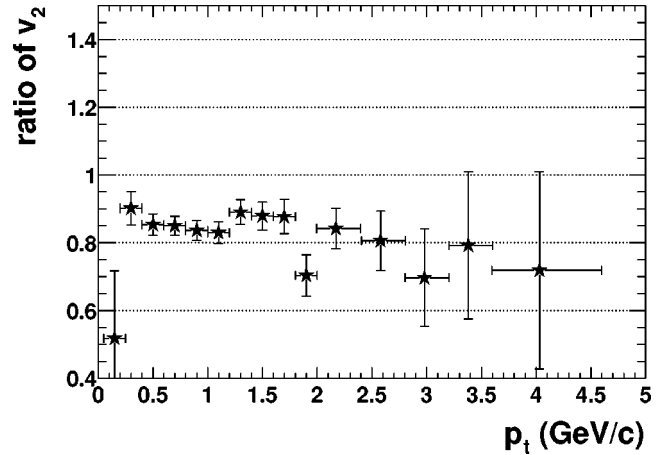

FIG. 18. The ratio of v_2 from the fourth-order cumulant divided by v_2, from the conventional method as a function of p_t, averaged over all centralities from bin 2–7, as defined in Figs. 14 and 15.

V. ELLIPTIC FLOW FLUCTUATIONS

High-precision results presented in this paper become sensitive to another effect usually neglected in flow analysis, namely, event-by-event flow fluctuations. The latter can have two different origins: "real" flow fluctuations—fluctuations at fixed impact parameter and fixed multiplicity (see, for example, Ref. [40])—and impact parameter variations among events from the same centrality bin in a case where flow does not fluctuate at fixed impact parameter. These effects, in principle, are present in any kind of analysis, including the "standard" one based on pair correlations. The reason is that any flow measurements are based on correlations between particles, and these very correlations are sensitive only to certain moments of the distribution in v_2. In the pair correlation approach with the reaction plane determined from the second harmonic, the correlations are proportional to v^2. After averaging over many events, one obtains $\langle v^2 \rangle$, which, in general, is not equal to $\langle v \rangle^2$. The four-particle cumulant
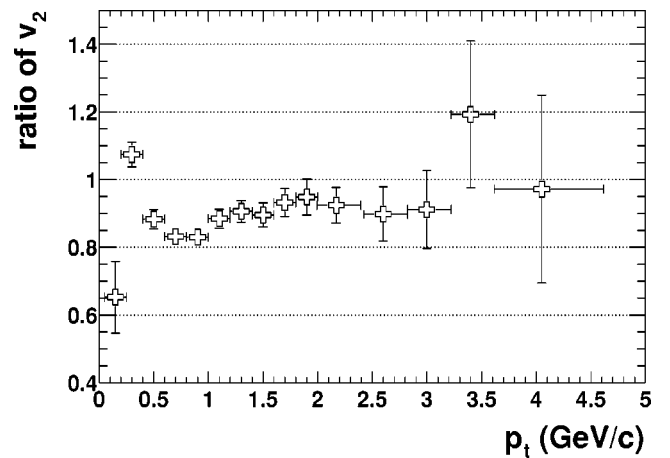

FIG. 19. The ratio of v_2 from quarter events divided by the conventional v_2 as a function of p_t. In both cases, event planes were constructed from low-p_t (<0.5 GeV/c) particles. The data are averaged over all centralities from bin 2–7, as defined in Figs. 14 and 15.
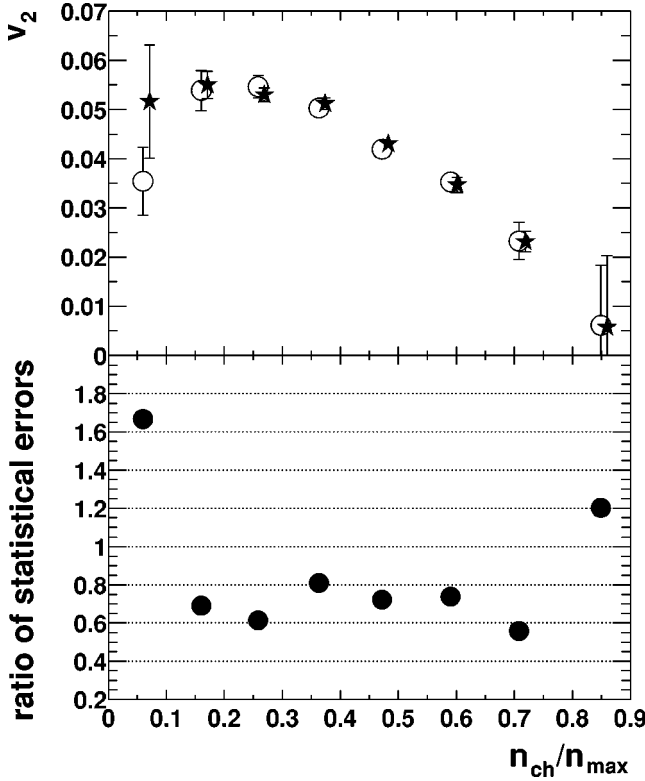
FIG. 20. The upper panel shows measured v_2 from fourth-order cumulants vs centrality with p_t weighting (stars) and unit weighting (circles). The bottom panel is the ratio of the error from p_t weighted v_2 to that of unit weighted v_2.

method involves the difference between four-particle correlations and (twice) the square of the two-particle correlations. In this paper, we assume that this difference comes from correlations in the nonflow category. Note, however, that in principle this difference ($\langle v^4 \rangle - \langle v^2 \rangle^2 \neq 0$) could be due to flow fluctuations. Let us consider an example where the distribution in v is flat from $v = 0$ to $v = v_{max}$. Then, a simple calculation would lead to the ratio of the flow values from the standard two-particle correlation method and four-particle cumulants as large as $\langle v^2 \rangle^{1/2} / (2 \langle v^2 \rangle^2 - \langle v^4 \rangle)^{1/4} = 5^{1/4} \approx 1.5$.

In this study, we consider the possible bias in elliptic flow measurements under the influence of impact parameter fluctuations within the studied centrality bins. The largest effect is expected within the bin of highest multiplicity, where the impact parameter and v_2 are both known *a priori* to fluctuate down to zero in the limit of the most central collisions. These fluctuations lead to bin-width-dependent bias in the extracted v_2 measurements.

In Sec. III, two approximations were made in order to extract the final flow result,

$$\langle v_n^4 \rangle \simeq \langle v_n^2 \rangle^2 \quad \text{and} \quad \langle v_n^2 \rangle \simeq \langle v_n \rangle^2.$$

Taking into account the centrality binning fluctuation on flow, namely, $\sigma_{v_n^2}^2$ and $\sigma_{v_n}^2$,
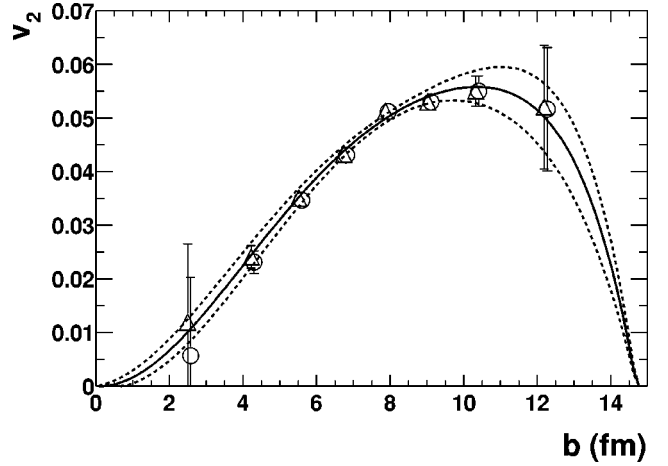

FIG. 21. v_2 as a function of the impact parameter. The data points are shown at the values of $\langle b \rangle$ for a given centrality bin. For the description of the fit procedure see text. The triangles are the final fourth-order cumulant data after correction for fluctuations as described in Sec. IV, while the circles show the fourth-order cumulant data before this correction. The dashed lines represent the estimated uncertainty in the parametrization represented by the solid curve.

$$\langle v_n^4 \rangle = \sigma_{v_n^2}^2 + \langle v_n^2 \rangle^2 \quad \text{and} \quad \langle v_n^2 \rangle = \sigma_{v_n}^2 + \langle v_n \rangle^2,$$

and Eq. (21) becomes

$$-v_n^4 - 2 \sigma_{v_n}^2 v_n^2 - \sigma_{v_n}^4 + \sigma_{v_n^2}^2 = -v_{\text{meas}}^4, \tag{29}$$

which is a function of v_n and is solvable for v_n, if $\sigma_{v_n}^2$ and $\sigma_{v_n^2}^2$ are known. A method of calculating both $\sigma_{v_n}^2$ and $\sigma_{v_n^2}^2$ is now presented.

First, we need to parametrize v_n as a function of impact parameter b. Consider a polynomial fit $v_n = a_0 + a_1 b + \cdots + a_6 b^6$, in which case the measured flow is $\langle v_n \rangle = a_0 + a_1 \langle b \rangle + \cdots + a_6 \langle b^6 \rangle$. The various averages $\langle b \rangle$, $\langle b^2 \rangle$, $\cdots, \langle b^{12} \rangle$ can be estimated in each centrality bin from filtered HIJING events. The parameters a_i have been determined by minimizing χ^2 in a fit to the eight $v_2(n_{ch})$ measurements. In addition, the fit is constrained to go through $v_2 = 0$ at $b = 0$ and at $b_{max} = 14.7$ fm [41]. The variation of b_{max} within ± 0.5 fm has a negligible effect on $v_2(b)$ at $b < 12$ fm. Figure 21 shows the resulting curve:

$$v_2(b) = -0.000\,394 b + 0.002\,10 b^2 - 0.000\,070\,6 b^3$$
$$-0.000\,032\,0 b^4 + 0.000\,003\,58 b^5 - 1.174 \times 10^{-7} b^6,$$
$$\tag{30}$$

where it is assumed that b is in femtometers. In principle, the final corrected $v_2(n_{ch})$ should be determined iteratively, but the result is stable on the first iteration.

Next we consider

$$\sigma_{v_n}^2 = \langle v_n^2 \rangle - \langle v_n \rangle^2 = (a_0^2 + 2a_0 a_1 \langle b \rangle + \cdots + a_6^2 \langle b^{12} \rangle)$$
$$- (a_0 + a_1 \langle b \rangle + \cdots + a_6 \langle b^6 \rangle)^2,$$
(31)

and again the various averages of powers of b can be estimated using HIJING.

After computing $\sigma_{v_n}^2$, $\sigma_{v_n^2}^2$, and obtaining v_{meas} from the four-particle correlation method, Eq. (29) can be solved to extract the v_n corrected for impact parameter fluctuations. The v_2 bias is found to be entirely negligible in all the studied centrality bins except for the most central, where the correction is about a factor of 2 (see the leftmost bin in Fig. 21). In the present analysis, even a factor of two is not significant due to the large statistical error on v_2 for maximum centrality. However, the correction to v_2 resulting from finite centrality bin width at maximum centrality has been determined with lower uncertainty than v_2 itself, and will become important in future studies with large samples of events.

Real event-by-event fluctuation in the flow coefficients would also make the four-particle values lower than the two-particle values. At the moment, there is no way to calculate this effect, although it is expected to be small.

VI. THE CENTRALITY DEPENDENCE OF ELLIPTIC FLOW

The centrality dependence of elliptic flow is a good indicator of the degree of equilibration reached in the reaction [42,43]. Following Ref. [41], we compute the initial spatial eccentricity for a Woods-Saxon distribution with a wounded nucleon model from

$$\varepsilon = \frac{\langle y^2 \rangle - \langle x^2 \rangle}{\langle y^2 \rangle + \langle x^2 \rangle},$$

where x and y are coordinates in the plane perpendicular to the beam and x denotes the in-plane direction. The method of calculation of ϵ is the same as that used for the hydro values [44]. The ratio v_2 / ε is of interest because it has been argued to be independent of centrality in a hydrodynamic model with a constant speed of sound [6]. In hydrodynamic model calculations using an equation of state with a phase transition (sound speed is not constant) this ratio does change as a function of centrality, however within the 10% level [44]. Hydrodynamics represents one possible limiting case in describing nuclear collisions—the limit where the mean free path for interaction of the constituents represented by the fluid cells is very small compared with the region of nuclear overlap. The opposite limit, where the mean free path is long (or at least comparable to the dimensions of the nuclear overlap region), is normally known as the low density limit (LDL). In nuclear transport models, the mean number of hard binary interactions per particle is typically small, and the predictions of these models tend to be closer to the low density limit than the hydro limit. In order to judge the proximity of measured flow data to either of these limits, it is useful to plot, as in Fig. 22, v_2 / ε versus charged particle
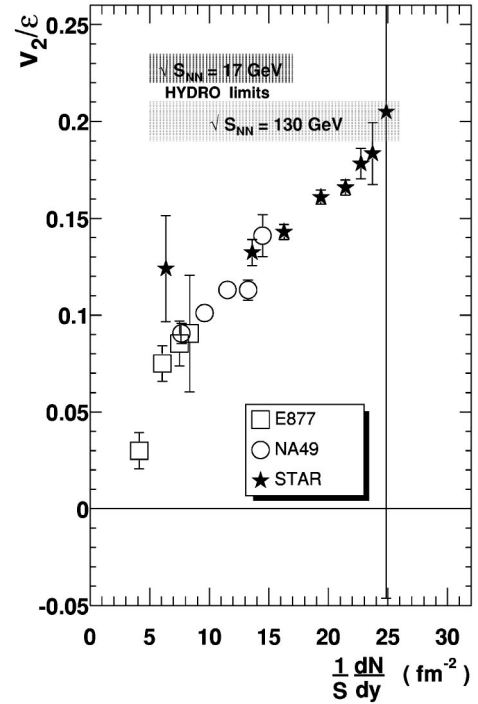

FIG. 22. v_2 / ε as a function of charged particle density in Au + Au collisions. Data are from E877 at the AGS (squares), NA49 at the SPS (circles), and STAR at RHIC (stars). The AGS and SPS data have been obtained by conventional flow analysis. The STAR measurements are at $\sqrt{s_{NN}} = 130$ GeV, and correspond to the final corrected elliptic flow based on fourth-order cumulants, and we assume $dN/dy = 1.15 dN/d\eta$. The horizontal shaded bands indicate the hydrodynamic limits for different beam energies [44].

density in the form $(dN/dy)/S$, where dN/dy is the rapidity density, and the area of the overlap region is $S = \pi \sqrt{\langle x^2 \rangle \langle y^2 \rangle}$ as computed above. Since v_2 / ε is proportional to $(dN/dy)/S$ in the LDL case [18,42], this form of the plot offers meaningful insights without reference to detailed theoretical models.

Figure 22 presents Au+Au data from AGS/E877 [45], from NA49 [43], as well as the current STAR measurements based on fourth-order cumulants, corrected for fluctuations as detailed in Sec. IV. Alternative forms of the centrality dependence readily can be generated using the tabulated quantities presented in Table I. Generally, the current STAR results underline the need for much increased statistics, particularly for the most central collisions. Within the uncertainties, a smooth trend of increasing v_2 / ε with increasing centrality [larger $(dN/dy)/S$] is observed, without the obvious kink that has been suggested as a phase transition signature [18,46]. Another proposed phase transition signature, which is not favored by the data, is a few percent rise in v_2 / ε with *decreasing* centrality [44]. It is worth noting that the v_2 / ε values reached in the most central RHIC collisions are consistent with the hydrodynamic limit [6,44,47], whereas v_2 / ε in central collisions at AGS and SPS is significantly lower. It is also worth noting that while the roughly linear relationship between v_2 / ε and $(dN/dy)/S$ across the presented beam energies and centralities is consistent with the LDL picture

[18], the measured $v_2(p_t)$, Fig. 15, cannot be explained by current LDL implementations [48], and is much closer to hydrodynamic calculations up to 2 GeV/c [48].

VII. CONCLUSION

In this work, we provide details of the approach for treating nonflow correlations within the framework of the standard elliptic flow analysis method based on particle pairs. We also compare the standard method with a new and simpler pair analysis based on the scalar product of flow vectors. The latter yields a 15%–35% reduction in statistical errors, with the best improvement occurring in the case of the most central and the most peripheral events.

It is concluded that four-particle correlation analyses can reliably separate flow and nonflow correlation signals, and the latter account for about 15% of the observed second-harmonic azimuthal correlation in year-one STAR data. The cumulant approach has demonstrated some advantages over the previous alternatives for treating nonflow effects. In particular, fourth-order cumulants allows us to present v_2 measurements fully corrected for nonflow effects, in contrast to the earlier analyses where the nonflow contribution was partly removed and partly quantified by the reported systematic uncertainties. It is observed that nonflow correlations are present in $\sqrt{s_{NN}} = 130$ GeV Au + Au events throughout the studied region $|\eta| < 1.3$ and $0.1 < p_t < 4.0$ GeV/c, and are present at all centralities. The largest contribution from nonflow correlations is found among the most peripheral and the most central collisions.

On the other hand, a fourth-order cumulant analysis is subject to larger statistical errors than a conventional pair correlation analysis of the same dataset. The total uncertainty on the fourth-order analysis, including both statistical and systematic effects, is smaller for year-one STAR data except in the most central and peripheral panels of Figs. 14 and 15. In the case of future studies of larger numbers of events, a higher-order analysis should provide an advantage in all cases.

Fluctuations within the studied multiplicity bins have the potential to bias elliptic flow results. This bias has been estimated and found to be entirely negligible except for the most central multiplicity bin, where the correction is about a factor of 2. In the present analysis, even this large a bias is only marginally significant, but again, this correction will presumably be important in future studies with much improved statistics.

We present STAR data for v_2/ε—elliptic flow in various centrality bins, divided by the initial spatial eccentricity for those centralities. Mapping centrality onto a scale of charged particle density enables us to study a broad range of this quantity, from peripheral AGS collisions, through SPS, and ending with central RHIC collisions. Within errors, the STAR data follow a smooth trend. No evidence for a softening of the equation of state or for a change in degrees of freedom has been observed. The three experiments at widely differing beam energies show good agreement in v_2/ε where they overlap in their coverage of particle density. The pattern of v_2/ε being roughly proportional to particle density continues over the density range explored at RHIC, which is consistent with a general category of models that approximate the low density limit as opposed to the hydrodynamic limit. Nevertheless, v_2/ε at STAR is consistent with having just reached the hydrodynamic limit for the most central collisions.

[1] W. Reisdorf and H. G. Ritter, Annu. Rev. Nucl. Part. Sci. **47**, 663 (1997).

[2] N. Herrmann, J. P. Wessels, and T. Wienold, Annu. Rev. Nucl. Part. Sci. **49**, 581 (1999).

[3] J.-Y. Ollitrault, Nucl. Phys. **A638**, 195c (1998).

[4] A. M. Poskanzer, nucl-ex/0110013.

[5] H. Sorge, Phys. Rev. Lett. **78**, 2309 (1997).

[6] J.-Y. Ollitrault, Phys. Rev. D **46**, 229 (1992).

[7] S. Voloshin and Y. Zhang, Z. Phys. C: Part. Fields **70**, 665 (1996).

[8] A. M. Poskanzer and S. A. Voloshin, Phys. Rev. C **58**, 1671 (1998).

[9] K. H. Ackermann *et al.*, STAR Collaboration, Phys. Rev. Lett. **86**, 402 (2001).

[10] D. Teaney, J. Lauret, and Edward V. Shuryak, Nucl. Phys. **A698**, 479 (2002).

[11] D. Teaney, J. Lauret, and Edward V. Shuryak, nucl-th/0110037.

[12] Zi-Wei Lin and C. M. Ko, Phys. Rev. C **65**, 034904 (2002).

[13] C. M. Ko, Zi-wei Lin, and S. Pal, Phys. Rev. C **65**, 034904 (2002).

[14] D. Molnar and M. Gyulassy, Nucl. Phys. **A697**, 495 (2002).

[15] E. E. Zabrodin, C. Fuchs, L. V. Bravina, and A. Faessler, Phys. Lett. B **508**, 184 (2001).

[16] T. J. Humanic, nucl-th/0205053.

[17] C. Adler *et al.*, STAR Collaboration, Phys. Rev. Lett. **87**, 182301 (2001).

[18] H. Heiselberg and A.-M. Levy, Phys. Rev. C **59**, 2716 (1999).

[19] J. Jiang *et al.*, Phys. Rev. Lett. **68**, 2739 (1992).

[20] N. Borghini, P. M. Dinh, and J.-Y. Ollitrault, Phys. Rev. C **63**, 054906 (2001).

[21] N. Borghini, P. M. Dinh, and J.-Y. Ollitrault, Phys. Rev. C **64**, 054901 (2001).

[22] K. H. Ackermann *et al.*, STAR Collaboration, Nucl. Phys. **A661**, 681c (1999).

[23] P. Danielewicz and G. Odyniec, Phys. Lett. **157B**, 146 (1985).

[24] M. Gyulassy and X.-N. Wang, Comput. Phys. Commun. **83**, 307 (1994); X.-N. Wang and M. Gyulassy, Phys. Rev. D **44**, 3501 (1991).

[25] P. Danielewicz, Phys. Rev. C **51**, 716 (1995).

[26] A. M. Poskanzer and S. A. Voloshin, LBNL Annual Report, 1998, http://ie.lbl.gov/nsd1999/rnc/RNC.htm

[27] J. Barrette *et al.*, E877 Collaboration, Phys. Rev. Lett. **73**, 2532 (1994).

[28] J.-Y. Ollitrault, Nucl. Phys. **A590**, 561c (1995).

[29] J.-Y. Ollitrault, nucl-ex/9711003.

[30] N. Borghini, P. M. Dinh, and J.-Y. Ollitrault, Phys. Rev. C **62**, 034902 (2000).

[31] P. M. Dinh, N. Borghini, and J.-Y. Ollitrault, Phys. Lett. B **477**, 51 (2000).

[32] M. Biyajima, Phys. Lett. **92B**, 193 (1980); Prog. Theor. Phys. **66**, 1378 (1981).

[33] R. L. Liboff, *Kinetic Theory* (Prentice-Hall, Englewood Cliffs, NJ, 1989).

[34] H. C. Eggers, P. Lipa, P. Carruthers, and B. Buschbeck, Phys. Rev. D **48**, 2040 (1993).

[35] N. Borghini, P. M. Dinh, and J.-Y. Ollitrault, nucl-ex/0110016.

[36] R. L. Ray and R. S. Longacre, nucl-ex/0008009.

[37] R. Snellings *et al.*, STAR Collaboration, Nucl. Phys. **A698**, 193c (2002).

[38] M. Gyulassy, I. Vitev, and X. N. Wang, Phys. Rev. Lett. **86**, 2537 (2001).

[39] C. Adler *et al.*, STAR Collaboration, nucl-ex/0206006.

[40] C. E. Aguiar *et al.*, Nucl. Phys. **A698**, 639c (2002).

[41] P. Jacobs and G. Cooper, nucl-ex/0008015.

[42] S. A. Voloshin and A. M. Poskanzer, Phys. Lett. B **474**, 27 (2000).

[43] A. M. Poskanzer and S. A. Voloshin, Nucl. Phys. **A661**, 341c (1999).

[44] P. F. Kolb, J. Sollfrank, and U. Heinz, Phys. Rev. C **62**, 054909 (2000).

[45] J. Barrette *et al.*, E877 Collaboration, Phys. Rev. C **51**, 3309 (1995); **55**, 1420 (1997).

[46] H. Sorge, Phys. Rev. Lett. **82**, 2048 (1999).

[47] P. Kolb, J. Sollfrank, and U. Heinz, Phys. Lett. B **459**, 667 (1999).

[48] P. F. Kolb, P. Huovinen, U. Heinz, and H. Heiselberg, Phys. Lett. B **500**, 232 (2001).